PET/MRI: Motion Correction

5

Ciprian Catana

Contents

5.1 Introduction

The theoretical spatial resolution of current-generation PET scanners can rarely be achieved in practice because of subject motion. Motion negatively impacts virtually all types of PET studies and can be broadly classified into rigid-body motion in which the whole organ of interest moves as a whole (e.g., brain) and nonrigid-body motion (e.g., cardiac, respiratory, bulk) in which deformations of the internal organs occur. The former is relevant in neurological studies, while the latter negatively

C. Catana
Athinoula A. Martinos Center for Biomedical Imaging, Department of Radiology,
Massachusetts General Hospital and Harvard Medical School, Charlestown, MA, USA
e-mail: ccatana@nmr.mgh.harvard.edu

degrades the quality of whole-body studies in oncology and cardiology. In addition to the "image blurring" effect that makes the characterization of small features of interest (e.g., cortical gray matter regions in neurology, primary or metastatic lesions in oncology, myocardial perfusion defects in cardiology) even more difficult, motion leads to bias in quantification and artifacts due to mismatches between the emission and attenuation data.

Recently, integrated PET/MRI scanners capable of simultaneous data acquisition have been introduced [1, 2] and used in numerous proof-of-principle studies in various patient populations, as discussed in the other chapters. Most of the methods previously proposed for motion control (i.e., gating or binning the acquisition into shorter frames that are minimally affected by motion) for both MR and PET are also available in these integrated devices. Although these techniques are not specifically reviewed in this chapter, we note that gating of the emission data is a required step for virtually all the MR-based motion correction approaches discussed. However, the obvious disadvantage of gating is that the signal-to-noise ratio (SNR) in the images obtained from short frames is significantly reduced as a large proportion of the recorded events are discarded. PET data-driven motion estimation has also been a highly researched topic with several promising methods having been developed over the last decades [3]. Although they could be used in integrated PET/MR scanners as we previously described [4], these approaches will not be covered in this chapter, and instead we will focus on the methods that have been specifically suggested in the context of PET/MRI. This novel technology allows the use of motion estimates derived from one modality to perform motion compensation of the data acquired with the other technique. The obvious example and the most widely explored direction to date is the use of MR-derived motion estimates for PET motion correction. However, a cross-modality validation of the motion estimates could be performed in an integrated device, and it is not unconceivable that PET-based estimates could eventually also be used to minimize the effects of motion on the MR images in certain scenarios.

	Displacement (mm)		
	Cranio-caudal	Anterior-posterior	Lateral
Lung lesions	10	9	8
Heart	3.8–23.5	−1.3 to 11.5	−1.8 to 6.1
Liver			
Normal inspiration	10 to 26	10	10
Deep inspiration	75		
Spleen	20	10	5
Pancreas tumor	13–42	3–13	
Kidney	2.5–20.5	0.6–8	0.4–5.9
Prostate	0.5–10.6	0.3–10	

There are several types of motion that negatively impact research and clinical PET/MRI studies [4]. Head motion is random and often occurs very rapidly but can be characterized by simple rigid-body rotations and translations. Respiratory motion

on the other hand can be assumed to be periodic, but it leads to nonrigid displacements of the internal organs in the thorax and abdomen. Furthermore, the amplitude of the motion depends on the type of respiration, with larger displacements being observed after a deep inspiration often used before breath-hold techniques. Even the path along which the various organs travel during inspiration is different than the one followed in expiration, a phenomenon termed hysteresis. The magnitudes of the respiratory-induced displacements for several internal organs (e.g., lung tumor [5], heart [6], liver [7–10], spleen [11], pancreas tumor [12, 13], kidney [14], prostate [15]) are summarized in the adjacent table (see [4] for a more detailed discussion). The motion of the heart throughout the cardiac cycle can also be assumed to be periodic but is very complex, involving longitudinal and radial contractions, as well as rotations of the apex and base in opposing directions [16]. Finally, bulk motion often occurs when patients adjust their position in the scanner. This "nonphysiological" motion is nonperiodic and leads to unpredictable displacements and deformations of the internal organs.

All these types of motion can be characterized using MR although the challenges and solutions are different in each case. For example, for head motion estimation, high temporal resolution methods are required to characterize the motion throughout the whole acquisition as no periodicity can be assumed, but the displacement of the head instead of each of the individual voxels is needed as the brain moves as a whole. On the other hand, periodic respiratory or cardiac motion can be modeled, but the motion vector fields that describe the displacements of all the voxels in the volume of interest have to be derived.

In the next sections, we will discuss several of the MR-based motion estimation and PET data correction strategies that have recently been proposed in the context of PET/MRI. It was not our intention to provide an exhaustive review of the literature and instead decided to focus on those methods that have the highest clinical potential, meaning they could be used routinely without minimal modification of the clinical protocols. First, the MR-based techniques for head, respiratory, cardiac, and bulk motion characterization will be introduced. Next, the algorithms for performing the actual PET data motion correction using these estimates will be briefly covered. Finally, the various methods proposed for the qualitative and quantitative assessment of the impact of motion correction on the PET data will be discussed.

5.2   MR-Based Motion Characterization

5.2.1   Head Motion

Numerous methods for estimating head motion from the MR have been developed but only a handful of them have been used in the context of PET/MR imaging. Head motion estimates can be derived from structural images acquired repeatedly (and ideally frequently) or from embedded navigators. The first human study that demonstrated that MR-based motion estimates can be used for PET motion correction was performed using the BrainPET prototype (Fig. 5.1) [17]. The echo planar
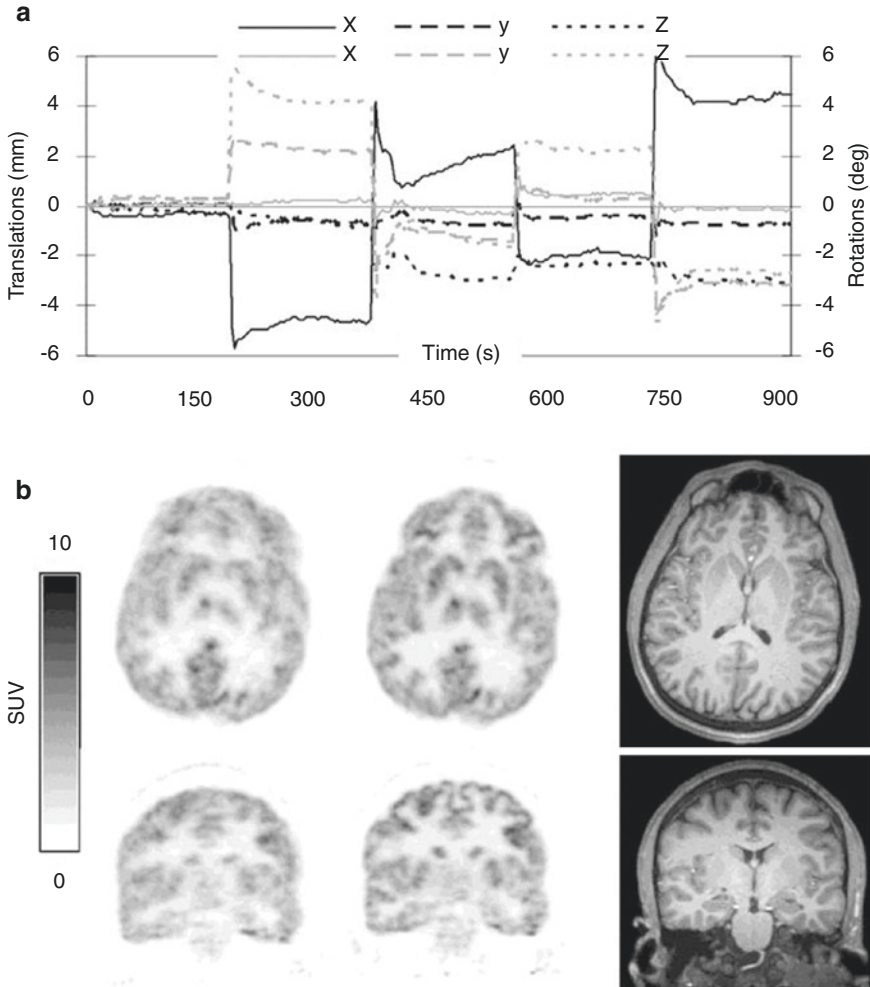
Fig. 5.1 MR-based motion correction in a healthy volunteer: (**a**) EPI-derived motion estimates obtained over a 15 min acquisition; (**b**) FDG PET images reconstructed before (left) and after motion correction (middle) and the corresponding MR images (right). Note the substantial improvement in PET image quality after motion correction. Figures originally published in The Journal of Nuclear Medicine [17]

imaging (EPI)-based estimates were obtained every time a complete volume was acquired (i.e., every 2–3 s). This concept is similar to the prospective acquisition correction (PACE) techniques [18] frequently used in functional MRI studies, except that the individual EPI volumes are coregistered offline using more accurate algorithms. Additionally, estimates were also obtained during high-resolution anatomic imaging using cloverleaf navigators [19]. Briefly, a k-space map was acquired at the beginning of the scan in 12 s. A short-duration (i.e., 20 ms) navigator inserted

every repetition time of a 3D-encoded fast low-angle shot (FLASH) sequence was used to estimate the transformation between the current head position relative to the initial map. These motion estimates were used for both prospective MR and retrospective PET data motion correction.

EPI-derived motion estimates were also used for PET motion correction by some of the other BrainPET early adopters [20–22]. Subsequently, the use of short 3D EPI volumetric navigators (vNavs) embedded in 3D multiecho magnetization-prepared rapid gradient-echo (MPRAGE), 3D T2-weighted sampling perfection with application optimized contrast using different flip angle evolution (SPACE), and 3D T2SPACE fluid-attenuated inversion recovery (FLAIR) sequences (routinely used to acquire high-resolution morphological brain data) was demonstrated to reduce the motion sensitivity of these sequences without degrading their performance [23]. The motion estimates derived from vNavs can be used for PET motion correction in the case of simultaneous PET/MR data acquisition.

Siemens introduced a head motion estimation and correction algorithm, called BrainCOMPASS, for the Biograph mMR scanner. It uses a PACE-based navigator [18] to obtain the head motion estimates simultaneously with the PET data acquisition in list-mode format. If the motion amplitude exceeds a certain threshold, the movement time and the corresponding translations and rotations are saved and later written into the DICOM header of the list-mode data.

A different approach for tracking the head motion involved wireless MR active markers [24] and dedicated MR sequences [25]. The wireless maker consists of a small NMR microsample bulb filled with doped water placed inside a matching size solenoid wireless MR coil. Using three such markers attached to the head of the subject is sufficient for characterizing the motion of the whole volume. A dedicated MR sequence is required to obtain the locations of the wireless markers by measuring their X, Y, and Z projections using separate gradient readouts along each of the directions.

5.2.2   Respiratory Motion

Respiratory motion characterization is a twofold problem. On one hand, a respiratory signal is required to bin the data into gates corresponding to the different phases of the respiratory cycle. On the other hand, a motion model [26] that characterizes the motion of the internal organs between these respiratory phases has to be generated. In the model generation phase, both the respiratory signal and the MR data required for calculating the model are acquired in the same time. Subsequently, only the respiratory signal is used to inform the application of the model, while other MR sequences are run.

The respiratory surrogate signal can be obtained using an external device such as a pressure sensor mounted in a chest belt that monitors the changes related to the displacement of the thoracic cage. Alternatively, navigator pulses derived directly from the MRI data could track the cranio-caudal motion of the right hemidiaphragm [27]. A more advanced method that can be used in the case of motion-insensitive

k-space sampling (e.g., radial or spiral trajectories) consists of deriving a self-gating signal from the k-space [28]. For example, in the case of a stack-of-stars trajectory in which radial sampling is performed in the k_{xy} plane at golden-angle increments and Cartesian sampling is performed in the k_z direction, the self-gating signal can be obtained from the central k-space partition. Additionally, the golden-angle acquisition allows the retrospective binning of the MR data into any desired number of gates. Good correlation between the respiratory signals generated from MR (and PET) data and those obtained from external devices has been reported [29].

To derive a respiratory model, a series of 2D images repeatedly acquired over several respiratory cycles can be used to generate the 3D volumes corresponding to the different respiratory phases [30–32]. Alternatively, these volumes can be obtained from the data collected with 3D radial stack-of-stars spoiled gradient-echo sequences and binned based on respiratory signal derived either from the k-space [28] or using a slice-projection navigator [33].

Once these 4D data (i.e., 3D volumes at multiple time points during the respiratory cycle) are available, various nonrigid registration algorithms (e.g., dense displacement sampling [34], demons [35], vector spline regularization [36], etc.) can be used to compute the motion vector fields between each of the respiratory gates and the reference gate.

Other MR motion estimation techniques such as tagged MRI, phase contrast MRI, and pulsed field gradient methods [37] have been proposed for estimating respiratory motion in the abdomen and thorax in early proof-of-principle PET/MRI studies. In fact, tagged MRI was first suggested in this context for tracking the respiratory motion in the abdomen, and proof-of-principle studies were performed in phantoms and animals [38, 39]. CSPAMM was used for tagging, while the motion fields were estimated using regularized HARP [38]. These methods will not be further discussed here because they have limited clinical potential, as they require long acquisition times and involve nondiagnostic MR sequences.

5.2.3   Cardiac Motion

Characterizing cardiac motion also requires a signal to divide the cardiac cycle into short frames (e.g., 50–100 ms). Although numerous techniques have been proposed for deriving a surrogate signal in MRI [40], the electrocardiogram (ECG)-based gating is the most widely used approach, being applied either prospectively or retrospectively. The latter method, in which data acquired continuously are time-stamped so that they can be retrospectively binned [41], is the one most relevant for motion estimation. Similar to the detection of the respiratory signal, cardiac self-gating can be used to obtain a cardiac signal directly from the k-space data [42, 43].

Once a cardiac signal is available and the data can be binned in different gates, a motion model to describe the transformations between the different cardiac phases needs to be generated.

MRI tagging is a technique that has been widely used in cardiac MRI, in which a virtual pattern (e.g., grid) is superimposed on the tissue of interest using a

selective radio-frequency pulse [44], through the spatial modulation of the magnetization (SPAMM) [45] or a train of RF pulses as in the delay alternating with nutation for tailored excitation (DANTE) sequence [46]. Contrast is thus introduced between the tagged and untagged voxels. The deformation of the tagging pattern is dependent on the motion of the underlying tissue, and various methods (e.g., active contour detection, optical flow, or template matching approaches) can be used to extract motion vector fields from these data. The feasibility of performing cardiac tagging on an integrated PET/MR scanner was first demonstrated using a cardiac beating phantom [47]. A SPAMM sequence was used for tagging the myocardium and nonrigid B-spline registration algorithm [48] for estimating the motion fields in all three directions from the tagged MRI volumes.

As already mentioned, one big disadvantage of the standard tagged MRI approach is that it requires long acquisition times. To address this limitation, accelerated tagged MRI using either parallel imaging (GRAPPA algorithm with up to four times acceleration) or compressed sensing (kt-FOCUSS algorithm) techniques has been suggested [49]. Furthermore, tagging is not useful for tracking the motion of structures on which the tags cannot be superimposed or fade very rapidly. This is the case when imaging the coronary arteries, which is of interest in patients with suspected coronary atherosclerotic disease. Obtaining the motion vector fields from the fat tissue that surrounds the whole heart has been suggested as an alternative [50].

A different framework for simultaneous respiratory motion-corrected cardiac MR angiography and PET imaging was recently developed [51]. The cardiac MR angiography data are acquired during free breathing but with ECG-triggering using a 3D T1-weighted spoiled gradient-echo sequence with a golden-step Cartesian spiral profile sampling trajectory. One spiral interleaf is acquired every cardiac cycle. The data acquired using a 2D image navigator repeated every cycle is used to estimate the translational motion in the foot-head and right-left direction. The respiratory signal obtained from the foot-head motion is used to bin the data into different respiratory phases, and the corresponding MR images are reconstructed using an iterative SENSE approach [52]. Finally, respiratory motion fields are obtained by nonrigidly registering the MR bins and applied to both the MR and PET data.

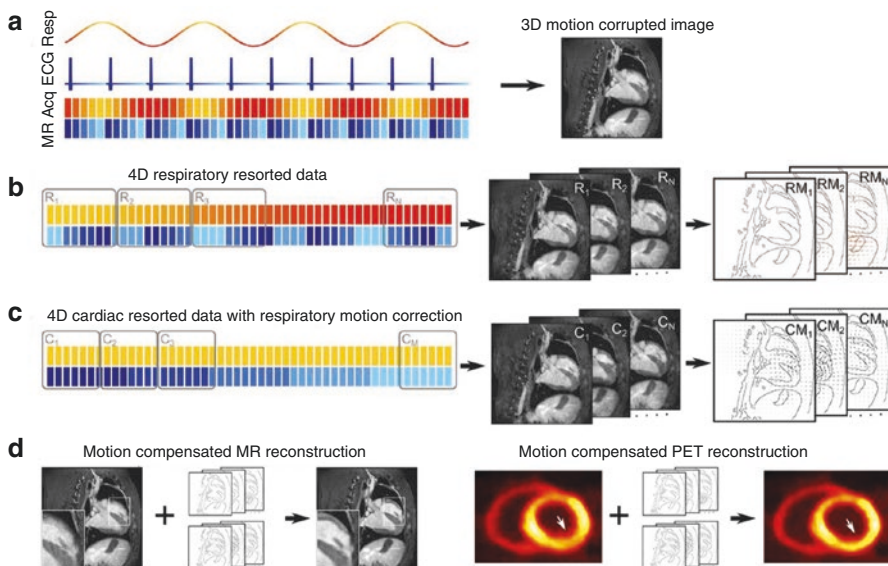## 5.2.4   Dual Respiratory and Cardiac Motion

Although the initial efforts in the PET/MRI field have focused on developing methods for compensating for respiratory and cardiac motion separately, both sources have to be addressed in the same time for in vivo cardiac studies. Dual gating can be performed using external devices to generate the bins required to capture the heart in the various phases along the respiratory and cardiac cycles. Simulation studies been performed to demonstrate the feasibility of dual motion estimation [50, 53].

An elegant approach recently proposed and assessed in vivo uses a 3D golden-radial phase encoding scheme [54]. The data are acquired over 5 min during free breathing and without ECG-triggering to cover several respiratory and cardiac cycles. The respiratory and cardiac signals are obtained from the k-space data using

the self-gating approach previously described and from an external ECG, respectively. The data are split into 8 respiratory and 12 cardiac motion states. Each acquired k-space spoke is assigned to a certain respiratory and cardiac motion state. The data are first reordered based on the respiratory motion states; the volumes corresponding to each respiratory state are reconstructed and registered to determine the respiration-induced heart motion. Next, respiratory motion is compensated for in the k-space, and the data are reordered based on the cardiac motion states. Finally, the motion-free volumes reconstructed from these data are nonrigidly coregistered to obtain the motion vector fields characterizing the motion of the heart during the cardiac cycle. This approach is summarized in Fig. 5.2.

In a different approach, respiratory and motion estimation is performed in two stages [53]. First, the respiratory-gated PET images are used to estimate the respiratory motion vector fields using a B-spline nonrigid registration algorithm and mean square difference as the cost function. These fields are then used to respiratory-motion correct the respiratory gates corresponding to each of the cardiac gates and generate respiratory motion-suppressed images in the reference phase. The cardiac-gated MR data are used to estimate the gate-to-gate cardiac motion vector fields that are finally used to cardiac-motion correct each of the respiratory motion-corrected cardiac gates.

Fig. 5.2 Respiratory and cardiac motion estimation and correction algorithm: (**a**) the MR data are labeled according to the respiratory (yellow-red) and cardiac (blue-cyan) motion states; (**b**) the 4D data are first sorted based on the respiratory labels and used to generate the 3D images corresponding to the N respiratory phases from which the respiratory motion fields (RM) are obtained; (**c**) in the next step, respiratory motion correction is performed, the k-space data are resorted based on the cardiac signal, and the M cardiac states obtained are used to calculate the cardiac motion fields (CM); (**d**) finally, dual motion compensation of the MR and PET data is performed. Figures originally published in *The Journal of Nuclear Medicine* [54]

5.2.5   Bulk Motion

MRI can also be used for detecting nonperiodic bulk motion such as that caused by the repositioning of the subject on the scanner table. In the only approach proposed to date, a 3D high-resolution radial phase encoding scheme was used to reconstruct MR images with three different temporal resolutions from the same data. The high temporal resolution images are used to detect the times when bulk motion occurs. Second, the "static" images between the detected time points are generated and used to estimate nonrigid-body motion vector fields between the different states. Finally, motion-compensated PET (and MR) images are reconstructed using the motion vector fields [55].

5.3   PET Data Motion Compensation Algorithms

5.3.1   Before Image Reconstruction

This class of methods was mainly used for rigid-body motion correction of the brain [17, 20–22]. In the motion compensation approach proposed in [17], the list-mode emission data acquired simultaneously with the MR data are first divided into frames of progressively longer duration according to the desired dynamic protocol. Each of these frames is subsequently divided into subframes based on the available MR-based motion estimates. The prompt and random events corresponding to each of the subframes are obtained in the line-of-response space by histogramming the list-mode data. Next, a reference position is selected (e.g., first subframe), and rigid-body transformation matrices for all the subsequent subframes are derived from the MR data. For each event detected in a particular line-of-response, the motion is accounted for by applying the transformer to the corresponding line and identifying the line-of-response in which the event should have been detected in the absence of motion using nearest neighbor interpolation. Alternatively, this can be viewed as "moving" the coordinates of all the crystals based on the transformer or that an event detected in a pair of crystals is assigned to a different pair of crystals based on the transformation matrix derived from the three rotations and three translations that define the rigid-body motion. Motion-compensated prompt and random event sinograms for each subframe are generated from these data. The emission data from all the subframes are added to obtain the motion-compensated prompt and random coincidence sinogram for each frame. The attenuation (and scatter) of the MR radio-frequency coil is accounted for separately since it is stationary with respect to the scanner. The motion-compensated sensitivity data are used to generate the normalization sinogram. Head attenuation and scatter correction sinogram are estimated only in the reference position. The motion-corrected PET volumes are reconstructed from these motion-compensated sinograms using the standard reconstruction algorithm.

A generic reconstruction library called PRESTO (PET reconstruction software toolkit) was proposed to transfer the data into a generic project space previous to

image reconstruction [22]. This approach avoids the degradation of motion-compensated projection data by the axial and transaxial compression that are typically performed for sinogram-based reconstruction. In an effort to reduce the computation time, a patient-specific algorithm to generate subframes only when the measured head displacement between two consecutive time points exceeds a certain threshold was subsequently suggested [21].

Although pre-reconstruction motion compensation algorithms are particularly useful for brain applications, it is worth noting that a similar approach could be used to perform respiratory motion compensation for cardiac studies as previously suggested [56] under the assumption that the heart moves rigidly with respiration.

5.3.2 During Image Reconstruction

The approach most often used for incorporating the MR-derived motion estimates is called motion-compensated image reconstruction (MCIR). Similar to the pre-reconstruction techniques, MCIR has the advantage that all the recorded events contribute to the final image, which leads to significantly improved counting statistics compared to the standard gating techniques in which the majority of the events are discarded. Furthermore, the Poisson nature of the data is maintained as opposed to the post-reconstruction techniques described in the next section.

To perform MCIR for whole-body applications, the PET data are first binned into to the desired number of respiratory or cardiac phases as described above. One of the gates is set as the reference position, and all the motion vector fields that transform the other gates into the reference position are obtained. The PET system matrix (that represents the probability of detecting in a specific line-of-response an event originating from a particular voxel) is modified to account for the nonrigid change in the activity distribution by applying a motion-warping operator [57]. Gate-specific attenuation maps are also generated from the MR-based attenuation map by applying the inverse transformations.

Several of the standard image reconstruction algorithms have been extended to incorporate motion vector fields into the system matrix in the context of PET/MRI such as the one-pass list-mode expectation maximization [31], maximum a posteriori (MAP) [33], maximum likelihood expectation maximization (MLEM) [38], and ordered-subsets expectation maximization (OSEM) [32, 58, 59]. An example of using MCIR for lung motion correction is shown in Fig. 5.3 [33].

Although most popular for whole-body applications, MCIR was also applied to head motion correction using vNav-derived motion estimates [60]. To optimize the computing resources, the list-mode data was adaptively binned into 4D sinograms based on the extent of motion. The mean voxel displacement in the imaging volume was calculated after each vNav acquisition and a new sinogram was generated whenever a threshold was exceeded. In order to account for motion, the authors used a 4D image reconstruction algorithm and a data augmentation method based on the alternating direction method of multipliers [61] that enabled to inclusion of a sparsity constraint to improve image quality.
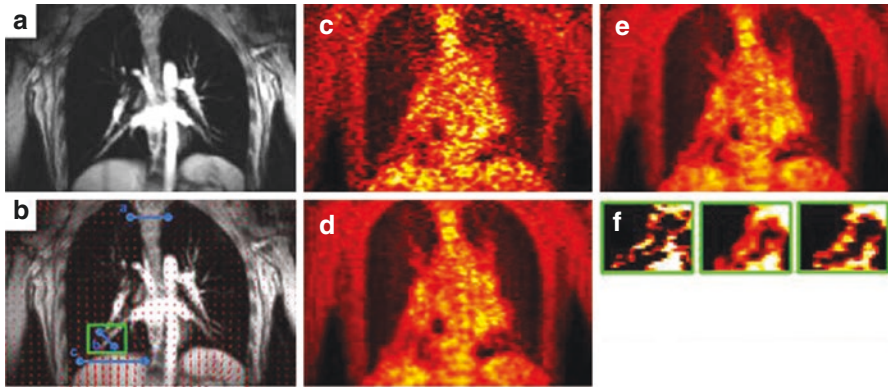
Fig. 5.3 Respiratory motion correction for lung imaging: (**a**) coronal MR image in the reference position and (**b**) overlaid deformation fields; (**c**) one-gated, (**d**) ungated, and (**e**) motion-corrected PET images; (**f**) magnified views of a blood vessel located near the diaphragm demonstrating significantly reduced blurring after motion correction. Figures originally published in *Medical Physics* [33]

5.3.3   After Image Reconstruction

Head motion correction post image reconstruction is used in the BrainCOMPASS approach proposed by Siemens. At the end of the acquisition, the PET data are binned into the motion states defined by the patient's movement exceeding the thresholds. The overall motion is limited to 20 mm (translation) and 8° (rotation). Up to 100 motion frames can be reconstructed. The original attenuation map is transformed to the position of each of the motion frames so that the attenuation correction is correctly performed. After all PET motion frames are reconstructed, the PET image volumes are transformed back to the position of a reference PET frame and summed together.

When using this approach for whole-body applications, the PET images corresponding to each of the gates are first reconstructed using the standard algorithms, and the MR-derived motion vector fields are applied to warp these images into the reference gate.

In one of the first proof-of-principle human studies that used an after image reconstruction approach, the PET gates were first reconstructed using the OSEM algorithm. The Dixon-based attenuation map acquired at end-expiration was warped using the MR-derived motion vector fields to obtain gate-specific attenuation maps. To generate the final image, the gated PET images were coregistered using the motion vector fields, scaled based on the total number of counts in each gate and summed on a voxel-by-voxel basis [30]. A similar approach was used in [28] except that the images corresponding to the individual gates were combined using weights proportional to the intra-bin amplitude range of the self-gating signal.

More recently, a post-reconstruction approach was used for free-breathing respiratory motion-corrected simultaneous cardiac MR angiography and PET

imaging [51]. The authors reconstructed each respiratory bin using the OSEM algorithm and gate-specific attenuation maps.

5.4   Performance Evaluation of MR-Based PET Motion Correction

5.4.1   Methods

There is currently no technique to serve as the gold standard for validating MR-based motion estimation approaches and no accepted metric for quantifying the impact of motion correction on the PET data. Several of the qualitative and quantitative approaches that have been proposed for this purpose in the proof-of-principle PET/ MRI studies are summarized in this section.

5.4.1.1 Head Motion

Substantial improvement in the FDG image quality was observed after MR-assisted motion correction in the first proof-of-principle study performed in a healthy volunteer [17]. A better delineation of brain structures and an apparent increase in gray matter uptake were observed after motion correction. Although the authors mainly focused on the static images generated from the data, images from 3 min subframes were also reconstructed and used to generate time activity curves for several gray matter structures. The shapes of these time activity curves were more similar to each other and consistent with the expected FDG kinetics only after motion correction.

Similar improvement in image quality and reduction of artifacts were observed in the brain phantom and patient studies subsequently performed on another BrainPET prototype [20, 21].

5.4.1.2 Respiratory Motion

Fayad et al. [31] compared the images obtained using the MCIR method to those produced using a post-reconstruction approach and the uncorrected ones. Data from 11 patients with metastatic lesions were included in the analysis. The qualitative analysis of the profiles drawn across the lesions showed good correlation between the motion-corrected images and differences compared to the uncorrected ones. The following figures of merit were selected for the quantitative analysis: differences in SNR (the signal and background noise were defined as the mean and standard deviation measured from ten 3 cm diameter regions of interest (ROIs) positioned across the liver), improvement in lesion-to-background contrast (mean lesion signal measured on the slice with the maximum count density and the background as the mean activity in a 3 cm diameter ROI placed in the background organ for each lesion), and full width at half maximum (FWHM) changes in lesion position and size. The improvements reported for the MCIR and post-reconstruction techniques were 28% and 24.2% mean SNR increases, 60.4% and 47.9% lesion size reduction, 70.1% and 57.2% lesion contrast increase, and 60.9% and 46.7% lesion position change, respectively.

Manber et al. [59] first validated the PET-derived respiratory signal against that obtained from the MR pencil-beam navigator on nine subjects who were imaged with either ^{18}F-FDG or ^{68}Ga-DOTATATE. The motion-corrected and uncorrected images were compared in four additional patients who underwent clinical PET/MRI scans. Increased sharpness for several of the lesions was observed by qualitatively examining the line profiles. The changes in standardized uptake values (SUVs) from a ROI defined in an area with high tracer uptake were chosen as the figure of merit for quantitative analysis. Mean increases in peak and maximum SUV of 23.1% and 34.5%, respectively, were observed in a patient with four pancreatic lesions.

Dutta et al. [33] performed simulation studies using the 4D XCAT phantom with 12 added spherical pulmonary lesions of 10 and 14 mm diameters. Three additional patients underwent PET/MRI scans to validate their motion correction framework. Bias and variance for the simulated lesions were evaluated for regularization parameters tuning. Additionally, the contrast-to-noise ratio (CNR, defined as the ratio of the sum of the means over the square root of the sum of the squared standard deviations (SDs) of the intensities in the ROI and background muscle tissue) was computed for high-intensity lung lesions. The authors also computed the mutual information between the features of interest in the PET images before and after motion correction and the corresponding features in the MR image. The bias was comparable for the one gate and motion-corrected images, while the standard deviation was higher for the former. The CNR was substantially improved for the latter.

Rank et al. [58] also performed simulations in addition to evaluating their algorithm in six patients with bronchial carcinoma. ROIs for every lesion were defined using a region-growing algorithm starting from the voxels with the maximum intensity. The SUV_{mean}, SUV_{max}, contrast (defined as the difference in the means in the lesion and background over the mean in the background), and SNR (defined as the difference in the means in the lesion and background over the standard deviation in the background) were calculated in these ROIs. Additionally, the lesion FWHM was calculated for the simulated data. Increases in SUV_{mean}, SUV_{max}, and contrast and a decrease of FWHM/lesion volume were reported for the motion compensation strategies. The SNR of the motion-corrected images was larger than that for the uncorrected case.

Manber et al. [32] evaluated the joint motion model generation method using data from 45 patients. The quantitative figures of merit were mutual information and sum of squared differences, Euclidean distance between deformation fields, and performance index that reflects percentage improvement. The motion compensation methodology was tested in five additional oncology patients who underwent PET-MRI studies. The PET image reconstruction improvements and artifact reduction were assessed visually, and increased sharpness was noted. The SUV_{max} and SUV_{peak} in avid lesion significantly increased after motion correction.

Munoz et al. [51] evaluated the motion-compensated cardiac MR angiography approach in ten subjects. Coronary vessel sharpness and length were used as metrics of MR image quality. The improvements reported were 37.9% and 49.1% for sharpness and 48.0% and 36.7% for length in the left and right coronary arteries, respectively. The PET motion correction strategy was evaluated in five oncology

patients. The PET images were analyzed by drawing profiles across the ventricle and by comparing the mean and coefficient of variation of the SUV in a myocardium ROI. The authors reported that the sharpness of the myocardium was improved after motion correction, while the noise was reduced compared to the gated images. Representative images from this study are shown in Fig. 5.4. The mean increased for three of the patients but remained almost constant for the other two after motion correction.

5.4.1.3 Cardiac Motion

In an effort to remove the influence of respiratory motion on cardiac studies, phantom and simulation studies were initially performed to study the effect of cardiac motion on the detection of cardiac lesions. For example, a beating nonrigid cardiac
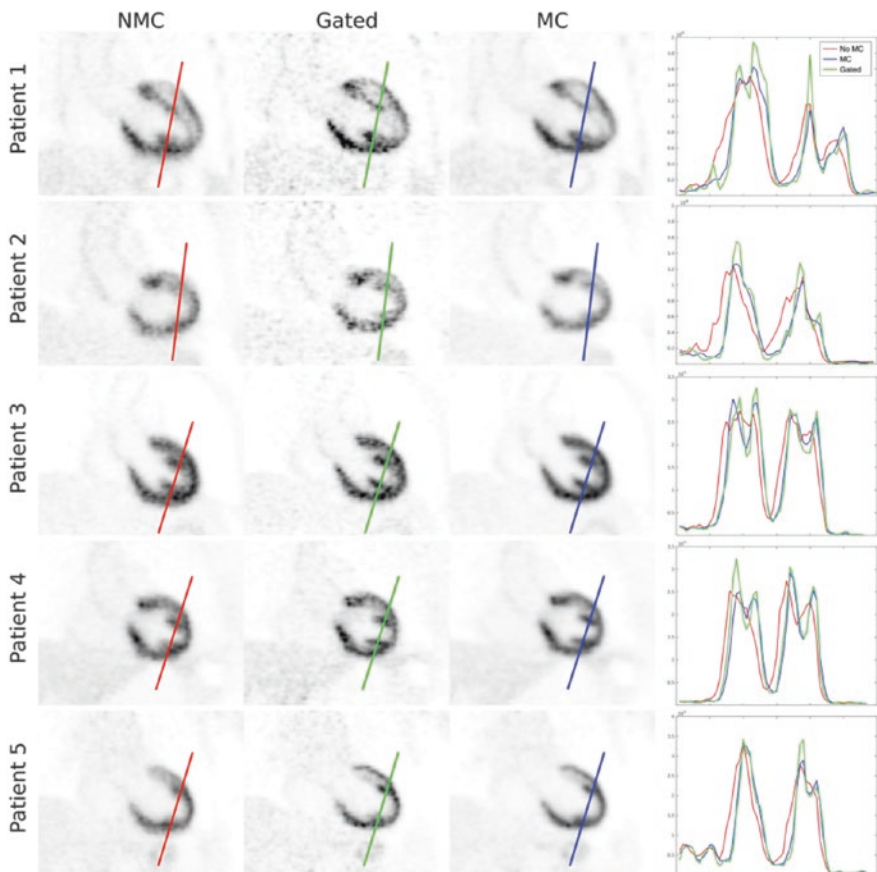
Fig. 5.4 Motion-corrected cardiac images. Coronal PET slices and profiles across the myocardium for five patients showing non-motion-corrected (NMC), gated, and motion-corrected (MC) images. MC improves myocardium sharpness compared to NMC and reduces noise compared to the gated reconstruction. Figures originally published in *Magnetic Resonance in Medicine* [51]

phantom filled with hot ^{18}F gel that also included cold gel inserts of different sizes to mimic transmural and non-transmural myocardial defects was used by Petibon et al. [47]. The defect/myocardium contrast recovery and image background statistical noise levels were compared between the different reconstructions. The authors also used a channelized Hotelling observer to perform a defect detectability study. Reduced spillover from the myocardium to background and defects was reported, leading to improved defect/myocardium contrast recovery (i.e., up to 206%). The improvement in lesion detectability ranged from 62% to 235% being dependent on the defect location (e.g., defects located in the lateral wall underwent the largest motion and demonstrated the largest improvement after motion compensation). These results were further improved after the incorporation of the scanner point spread function in the reconstruction [47].

The same group recently reported the results of a follow-up study in which they assessed the impact of motion and partial volume effects corrections on PET myocardial perfusion imaging in healthy pigs that underwent simultaneous dynamic ^{18}F-Flurpiridaz PET/MRI examinations. As respiratory-induced heart motion is minimal in this particular model, respiratory motion was not performed. Segment- and voxel-wise myocardial blood flow maps were obtained from the dynamic data using a two-tissue compartment model. The 17 American Heart Association (AHA) segments were analyzed. Myocardium-to-blood concentration ratios and wall thickness along profiles in the inferior-superior direction at various positions were estimated. When compared to the uncorrected data, the mean myocardium-to-blood ratio was increased by 20.3% and 13.6% for the motion-corrected and gated data, respectively. The mean apparent myocardial wall thickness was significantly lower after motion correction and gating. Similarly, the myocardial blood flow values were higher in these cases, although the variability was also increased for the gated images. As in the phantom study above, location-dependent differences in mean myocardial blood flow values were reported between the methods [62].

5.4.1.4 Dual Cardiac and Respiratory Motion

Simulation studies have shown that dual motion correction could improve the detection of atherosclerotic plaques [50] and myocardial perfusion defects [53]. Plaque- and defect-to-background contrast were used as the contrast metrics, and receiver operating characteristic analyses using channelized Hotelling observers were performed to study the effect of motion correction on the plaque/defect detectability.

Kolbitsch et al. [54] assessed the improvement in image quality and diagnostic accuracy using five dogs (myocardial infarction model) and one human subject. A qualitative assessment of myocardial uptake was performed using the AHA 17-segment bull's-eye plot. Quantitatively, the FWHM and CNR (defined as the difference between peak myocardial signal and mean blood pool signal over the SD of the latter) of the tracer uptake in the myocardium were estimated at locations that exhibited high cardiac motion in all the animals. When comparing the motion-corrected and uncorrected images of the canine myocardium, the FWHM and CNR improvement was 13% ± 5% and 90% ± 57%, respectively. Similar values (i.e., 18% and 103%, respectively) were reported for the human subject. Additionally, the

sharpness of the right coronary artery was measured from the MR images. An 85% ± 72% increase was reported after motion correction.

5.5   Beyond Proof-of-Principle Studies

Not surprisingly, most of the early research efforts in this field were aimed at demonstrating the feasibility of performing motion correction for various applications and assessing its potential impact on PET data qualitative and quantitative analyses. The focus has been slowly shifting to implementing practical methods that could be used for routine research studies and the hope is that such techniques will eventually be clinically useful. The first requirement for this to happen is to develop techniques in which the data needed for motion characterization are acquired efficiently or in the background of the sequences used for clinical purposes. While some of the early methods required long acquisition time that prevented the acquisition of clinical MR sequences [38, 39], the more recent ones allow the generation of the motion model from the data acquired in only 1 min [58, 59], or clinically relevant MR images can be obtained from the same data [51, 54]. Second, the quantitative accuracy of the PET data should be preserved, which seems to be the case as the consensus in the field is that quantification is actually improved after motion correction. Third, the data processing and image reconstruction time should be comparable to that of the current algorithms when using similar hardware, which is still challenging because the computational requirements for motion estimation/correction are extremely high. Fourth, studies with larger number of patients and in different clinical scenarios need to be performed to validate the various motion estimation/correction techniques. Fifth, additional MR sequences that allow the simultaneous acquisition of the information needed for characterizing the motion and that required for clinical purposes have to be implemented and validated. Finally, the major equipment manufacturers need to make these advanced algorithms available on their scanners and streamline them so that even non-experts can use them. Encouragingly, the head motion correction algorithm BrainCOMPASS is already commercially available on the Siemens Biograph mMR scanner, and recently, an extension of this technique, called BodyCOMPASS, has been introduced to enable motion-free imaging in other body regions such as the abdomen (similar to [28]).

For the BrainPET prototype, we have developed a package for automatic data processing and image reconstruction, called Masamune [63], that, among other capabilities, allows non-expert users to estimate the head motion from the MR data and generate MR-based motion-corrected dynamic frames. This allows head motion correction to be routinely used for research studies performed at the Martinos Center. Most recently, we performed MR-based head motion correction for studying the interaction between dopamine signaling and neural networks changes during working memory [64] and investigating the involvement of the dopaminergic system in the mechanisms of maternal bonding [65]. In a different study focusing on Alzheimer' disease patients, preliminary results showed the variability in the PET estimation of the cerebral metabolic rate of glucose is reduced after motion

correction [66], suggesting that PET data optimization may enable more careful assessment of subtle changes in brain metabolism and allow for reduced sample sizes in future research studies and clinical trials.

In conclusion, the feasibility of performing MR-based PET motion correction for brain and whole-body applications has been demonstrated. Several "practical" MR-based methods to estimate the motion that could be used routinely in research and clinical studies have already been proposed. Virtually all the proof-of-principle studies performed to date have shown that the quality of the PET (and in many cases of the MR) images substantially improves after motion correction, suggesting that MR-based motion correction could be a game changer in the PET/MR field much the same way CT-based attenuation correction has proven in the PET/CT field [67, 68].

References

1. Drzezga A, Souvatzoglou M, Eiber M, et al. First clinical experience with integrated whole-body PET/MR: comparison to PET/CT in patients with oncologic diagnoses. J Nucl Med. 2012;53:845–55.
2. Levin C, Glover G, Deller T, et al. Prototype time-of-flight PET ring integrated with a 3 T MRI system for simultaneous whole-body PET/MR imaging. J Nucl Med. 2013;54:148.
3. Kesner AL, Schleyer PJ, Büther F, et al. On transcending the impasse of respiratory motion correction applications in routine clinical imaging – a consideration of a fully automated data driven motion control framework. EJNMMI Phys. 2014;1:8.
4. Catana C. Motion correction options in PET/MRI. Semin Nucl Med. 2015;45:212–23.
5. Allen AM, Siracuse KM, Hayman JA, et al. Evaluation of the influence of breathing on the movement and modeling of lung tumors. Int J Radiat Oncol Biol Phys. 2004;58:1251–7.
6. McLeish K, Hill DL, Atkinson D, et al. A study of the motion and deformation of the heart due to respiration. IEEE Trans Med Imaging. 2002;21:1142–50.
7. Suramo I, Paivansalo M, Myllyla V. Cranio-caudal movements of the liver, pancreas and kidneys in respiration. Acta Radiol Diagn. 1984;25:129–31.
8. Korin HW, Ehman RL, Riederer SJ, et al. Respiratory kinematics of the upper abdominal organs - a quantitative study. Magn Reson Med. 1992;23:172–8.
9. Clifford MA, Banovac F, Levy E, et al. Assessment of hepatic motion secondary to respiration for computer assisted interventions. Comput Aided Surg. 2002;7:291–9.
10. Shimizu S, Shirato H, Aoyama H, et al. High-speed magnetic resonance imaging for four-dimensional treatment planning of conformal radiotherapy of moving body tumors. Int J Radiat Oncol Biol Phys. 2000;48:471–4.
11. Brandner ED, Wu A, Chen H, et al. Abdominal organ motion measured using 4D CT. Int J Radiat Oncol Biol Phys. 2006;65:554–60.
12. Feng M, Balter JM, Normolle D, et al. Characterization of pancreatic tumor motion using cine MRI: surrogates for tumor position should be used with caution. Int J Radiat Oncol Biol Phys. 2009;74:884–91.
13. Mori S, Hara R, Yanagi T, et al. Four-dimensional measurement of intrafractional respiratory motion of pancreatic tumors using a 256 multi-slice CT scanner. Radiother Oncol. 2009;92:231–7.
14. Yamashita H, Yamashita M, Futaguchi M, et al. Individually wide range of renal motion evaluated by four-dimensional computed tomography. SpringerPlus. 2014;3:131.
15. Dinkel J, Thieke C, Plathow C, et al. Respiratory-induced prostate motion: characterization and quantification in dynamic MRI. Strahlenther Onkol. 2011;187:426–32.
16. Sengupta PP, Korinek J, Belohlavek M, et al. Left ventricular structure and function: basic science for cardiac imaging. J Am Coll Cardiol. 2006;48:1988–2001.

17. Catana C, Benner T, van der Kouwe A, et al. MRI-assisted PET motion correction for neuro-logic studies in an integrated MR-PET scanner. J Nucl Med. 2011;52:154–61.
18. Thesen S, Heid O, Mueller E, et al. Prospective acquisition correction for head motion with image-based tracking for real-time fMRI. Magn Reson Med. 2000;44:457–63.
19. van der Kouwe AJW, Benner T, Dale AM. Real-time rigid body motion correction and shim-ming using cloverleaf navigators. Magn Reson Med. 2006;56:1019–32.
20. Scheins J, Ullisch M, Tellmann L, et al. MR-guided PET motion correction in LOR space using generic projection data for image reconstruction with PRESTO. Nucl Instrum Methods Phys Res Sect A. 2013;702:64–6.
21. Ullisch MG, Scheins J, Weirich C, et al. MR-guided data framing for PET motion correction in simultaneous MR-PET: a preliminary evaluation. Nucl Instrum Methods Phys Res Sect A. 2013;702:67–9.
22. Ullisch MG, Scheins JJ, Weirich C, et al. MR-based PET motion correction procedure for simultaneous MR-PET neuroimaging of human brain. PLoS One. 2012;7:e48149.
23. Tisdall MD, Hess AT, Reuter M, et al. Volumetric navigators for prospective motion correction and selective reacquisition in neuroanatomical MRI. Magn Reson Med. 2012;68:389–99.
24. Ackerman JL, Offutt MC, Buxton RB, et al. Rapid 3D tracking of small RF coils. Paper pre-sented at: Proceedings of the 5th annual meeting of SMRM, Montreal, Canada. 1986.
25. Huang C, Ackerman JL, Petibon Y, et al. Motion compensation for brain PET imaging using wireless MR active markers in simultaneous PET-MR: phantom and non-human primate stud-ies. NeuroImage. 2014;91:129–37.
26. McClelland JR, Hawkes DJ, Schaeffter T, et al. Respiratory motion models: a review. Med Image Anal. 2013;17:19–42.
27. Ehman RL, Felmlee JP. Adaptive technique for high-definition MR imaging of moving struc-tures. Radiology. 1989;173:255–63.
28. Grimm R, Furst S, Dregely I, et al. Self-gated radial MRI for respiratory motion compensation on hybrid PET/MR systems. Med Image Comput Comput Assist Interv. 2013;16:17–24.
29. Furst S, Grimm R, Hong I, et al. Motion correction strategies for integrated PET/MR. J Nucl Med. 2015;56:261–9.
30. Wurslin C, Schmidt H, Martirosian P, et al. Respiratory motion correction in oncologic PET using T1-weighted MR imaging on a simultaneous whole-body PET/MR system. J Nucl Med. 2013;54:464–71.
31. Fayad H, Schmidt H, Wuerslin C, et al. Reconstruction-incorporated respiratory motion cor-rection in clinical simultaneous PET/MR imaging for oncology applications. J Nucl Med. 2015;56:884–9.
32. Manber R, Thielemans K, Hutton BF, et al. Joint PET-MR respiratory motion models for clini-cal PET motion correction. Phys Med Biol. 2016;61:6515–30.
33. Dutta J, Huang C, Li Q, et al. Pulmonary imaging using respiratory motion compensated simultaneous PET/MR. Med Phys. 2015;42:4227–40.
34. Heinrich MP, Jenkinson M, Brady SM, et al. Globally optimal deformable registration on a minimum spanning tree using dense displacement sampling. In: Ayache N, Delingette H, Golland P, Mori K, editors. Medical image computing and computer-assisted intervention – MICCAI 2012: 15th international conference, Nice, France, October 1–5, 2012, proceedings, part III. Berlin, Heidelberg: Springer; 2012. p. 115–22.
35. Kroon DJ, Slump CH. MRI modality transformation in demon registration. Paper presented at: 2009 IEEE International Symposium on Biomedical Imaging: From Nano to Macro; June 28–July 1 2009. 2009.
36. Sorzano COS, Thévenaz P, Unser M. Elastic registration of biological images using vector-spline regularization. IEEE Trans Biomed Eng. 2005;52:652–63.
37. Ozturk C, Derbyshire JA, McVeigh ER. Estimating motion from MRI data. Proc IEEE. 2003;91:1627–48.
38. Guerin B, Cho S, Chun SY, et al. Nonrigid PET motion compensation in the lower abdomen using simultaneous tagged-MRI and PET imaging. Med Phys. 2011;38:3025–38.

39. Chun SY, Reese TG, Ouyang JS, et al. MRI-Based nonrigid motion correction in simultaneous PET/MRI. J Nucl Med. 2012;53:1284–91.
40. Scott AD, Keegan J, Firmin DN. Motion in cardiovascular MR imaging. Radiology. 2009;250:331–51.
41. Lenz GW, Haacke EM, White RD. Retrospective cardiac gating: a review of technical aspects and future directions. Magn Reson Imaging. 1989;7:445–55.
42. Larson AC, White RD, Laub G, et al. Self-gated cardiac cine MRI. Magn Reson Med. 2004;51:93–102.
43. Crowe ME, Larson AC, Zhang Q, et al. Automated rectilinear self-gated cardiac cine imaging. Magn Reson Med. 2004;52:782–8.
44. Zerhouni EA, Parish DM, Rogers WJ, et al. Human-heart-tagging with MR imaging - a method for noninvasive assessment of myocardial motion. Radiology. 1988;169:59–63.
45. Axel L, Dougherty L. MR imaging of motion with spatial modulation of magnetization. Radiology. 1989;171:841–5.
46. Mosher TJ, Smith MB. A DANTE tagging sequence for the evaluation of translational sample motion. Magn Reson Med. 1990;15:334–9.
47. Petibon Y, Ouyang J, Zhu X, et al. Cardiac motion compensation and resolution modeling in simultaneous PET-MR: a cardiac lesion detection study. Phys Med Biol. 2013;58:2085.
48. Ledesma-Carbayo MJ, Derbyshire JA, Sampath S, et al. Unsupervised estimation of myocardial displacement from tagged MR sequences using nonrigid registration. Magn Reson Med. 2008;59:181–9.
49. Huang C, Petibon Y, Ouyang J, et al. Accelerated acquisition of tagged MRI for cardiac motion correction in simultaneous PET-MR: phantom and patient studies. Med Phys. 2015;42:1087–97.
50. Petibon Y, El Fakhri G, Nezafat R, et al. Towards coronary plaque imaging using simultaneous PET-MR: a simulation study. Phys Med Biol. 2014;59:1203–22.
51. Munoz C, Neji R, Cruz G, et al. Motion-corrected simultaneous cardiac positron emission tomography and coronary MR angiography with high acquisition efficiency. Magn Reson Med. 2017. doi:10.1002/mrm.26690.
52. Pruessmann KP, Weiger M, Scheidegger MB, et al. SENSE: Sensitivity encoding for fast MRI. Magn Reson Med. 1999;42:952–62.
53. Wang X, Rahmim A, Tang J. MRI assisted dual motion correction for myocardial perfusion defect detection in PET imaging. Med Phys. 2017;44(9):4536–47. doi: 10.1002/mp.12429.
54. Kolbitsch C, Ahlman MA, Davies-Venn C, et al. Cardiac and respiratory motion correction for simultaneous cardiac PET/MR. J Nucl Med. 2017;58:846–52.
55. Kolbitsch C, Prieto C, Tsoumpas C, et al. A 3D MR-acquisition scheme for nonrigid bulk motion correction in simultaneous PET-MR. Med Phys. 2014;41:082304.
56. Livieratos L, Stegger L, Bloomfield PM, et al. Rigid-body transformation of list-mode projection data for respiratory motion correction in cardiac PET. Phys Med Biol. 2005;50:3313–22.
57. Lamare F, Ledesma Carbayo MJ, Cresson T, et al. List-mode-based reconstruction for respiratory motion correction in PET using non-rigid body transformations. Phys Med Biol. 2007;52:5187–204.
58. Rank CM, Heusser T, Wetscherek A, et al. Respiratory motion compensation for simultaneous PET/MR based on highly undersampled MR data. Med Phys. 2016;43:6234.
59. Manber R, Thielemans K, Hutton BF, et al. Practical PET respiratory motion correction in clinical PET/MR. J Nucl Med. 2015;56:890–6.
60. Pedemonte S, Catana C, Van Leemput K. 4-D PET-MR with volumetric navigators and compressed sensing. In: Gao F, Shi K, Li S, editors. Computational methods for molecular imaging. Cham: Springer; 2015. p. 93–101.
61. Boyd S, Parikh N, Chu E, et al. Distributed optimization and statistical learning via the alternating direction method of multipliers. Found Trends® Mach Learn. 2011;3:1–122.

62. Petibon Y, Guehl NJ, Reese TG, et al. Impact of motion and partial volume effects correction on PET myocardial perfusion imaging using simultaneous PET-MR. Phys Med Biol. 2017;62:326–43.

63. Chonde DB, Izquierdo-Garcia D, Chen K, et al. Masamune: a tool for automatic dynamic PET data processing, image reconstruction and integrated PET/MRI data analysis. EJNMMI Phys. 2014;1:A57.

64. Roffman JL, Tanner AS, Eryilmaz H, et al. Dopamine D-1 signaling organizes network dynamics underlying working memory. Sci Adv. 2016;2:10.

65. Atzil S, Touroutoglou A, Rudy T, et al. Dopamine in the medial amygdala network mediates human bonding. Proc Natl Acad Sci U S A. 2017;114:2361–6.

66. Chen KT, Hutchcroft W, Salcedo S, et al. Improved quantification of dementia PET data using temporally and spatially correlated MR data. In: World molecular imaging conference. New York, NY. 2016.

67. Townsend DW, Carney JP, Yap JT, et al. PET/CT today and tomorrow. J Nucl Med. 2004;45(Suppl 1):4S–14S.

68. Kinahan PE, Townsend DW, Beyer T, et al. Attenuation correction for a combined 3D PET/CT scanner. Med Phys. 1998;25:2046–53.